

## Research



**Cite this article:** Tiani R, Rongy L. 2023 Marangoni-driven nonlinear dynamics of bimolecular frontal systems: a general classification for equal diffusion coefficients. *Phil. Trans. R. Soc. A* **381**: 20220080. <https://doi.org/10.1098/rsta.2022.0080>

Received: 4 September 2022

Accepted: 14 November 2022

One contribution of 18 to a theme issue 'New trends in pattern formation and nonlinear dynamics of extended systems'.

**Subject Areas:**

chemical physics, physical chemistry, fluid mechanics, mathematical modelling

**Keywords:**

chemical front, reaction–diffusion–convection processes, Marangoni flow, surface tension, reaction reversibility

**Authors for correspondence:**

R. Tiani

e-mail: [reda.tiani@ulb.be](mailto:reda.tiani@ulb.be)

L. Rongy

e-mail: [laurence.rongy@ulb.be](mailto:laurence.rongy@ulb.be)

# Marangoni-driven nonlinear dynamics of bimolecular frontal systems: a general classification for equal diffusion coefficients

R. Tiani and L. Rongy

Nonlinear Physical Chemistry Unit, Université libre de Bruxelles (ULB), Faculté des Sciences, CP231, 1050 Brussels, Belgium

RT, 0000-0002-4070-565X; LR, 0000-0002-3556-7045

When bimolecular fronts form in solutions, their dynamics is likely to be affected by chemically driven convection such as buoyancy- and Marangoni-driven flows. It is known that front dynamics in the presence of buoyancy-driven convection can be predicted solely on the basis of the one-dimensional reaction–diffusion concentration profiles but that those predictions fail for Marangoni-driven convection. With a two-dimensional reaction–diffusion–Marangoni convection model, we analyze here convective effects on the time scalings of the front properties, together with the influence of reaction reversibility and of the ratio of initial reactants' concentrations on the front dynamics. The effect of buoyancy forces is here neglected by assuming the reactive system to be in zero-gravity condition and/or the solution density to be spatially homogenous.

This article is part of the theme issue 'New trends in pattern formation and nonlinear dynamics of extended systems'.

## 1. Introduction

When the reactants of a bimolecular reaction are initially separated, a chemical front forms and can propagate due to the interplay of reaction and transport processes. By gelling the medium in which the reaction occurs,

convection is prevented so that the only transport mechanism is diffusion. In this case, the dynamical properties of the resulting  $A + B \rightarrow C$  reaction–diffusion (RD) fronts that exhibit particular time scalings are well understood.

In particular, the front width and position scale with time as  $w \sim t^{1/6}$  and  $x_f \sim t^{1/2}$ , respectively, in the asymptotic long-time limit (diffusion-limited regime) [1]. More precisely, the front position (defined as the position of maximum reaction rate) can be written as  $x_f(t) = C_f \sqrt{t}$ , where  $C_f = C_f(b_0/a_0, D_a, D_b)$  determines the front direction, with  $a_0$  and  $b_0$  the initial concentrations of reactants A and B, respectively, and  $D_a, D_b$  their diffusion coefficients. The sign of  $C_f$  is determined by the sign of  $(a_0\sqrt{D_a})/(b_0\sqrt{D_b}) - 1$ . For an initial condition corresponding to A and B in the negative and positive  $x$  regions, respectively,  $C_f > 0$  and the front propagates to the right ( $x_f > 0$ ) when  $a_0\sqrt{D_a} > b_0\sqrt{D_b}$  and vice versa. In particular, the front is shown to be stationary when  $C_f = 0$ , i.e. when  $a_0\sqrt{D_a} = b_0\sqrt{D_b}$ . While the aforementioned results apply for purely irreversible RD systems, Chopard *et al.* extended the analysis for the reversible  $A + B \rightleftharpoons C$  case [2]. The authors found a crossover between the classical irreversible scalings and the reversible ones at a time proportional to  $1/g$ , where  $g$  is the backward rate constant. When  $t \gg 1/g$  (reversible regime), a state of local equilibrium is reached in the reaction zone and both the front width and position scale as  $t^{1/2}$ .

In gel-free experiments, spontaneous macroscopic motions of the fluid (convective motions) can arise and lead to new dynamical scenarios [3–5]. When a chemical front propagates horizontally, i.e. perpendicularly to the gravity field, in systems open to the air, surface tension and density gradients across the reaction zone can induce buoyancy- and Marangoni-driven convection, respectively (see review in [6]).

When the front is only influenced by buoyant forces, with  $a_0 = b_0$  and  $D_a = D_c = D_b$  (with  $D_c$  the diffusion coefficient of species C), the reaction–diffusion–convection (RDC) front dynamics can be predicted solely from the one-dimensional RD density profiles and the front motion is directed towards the region with smallest density gradient [7]. For unequal initial concentrations of reactants ( $a_0 \neq b_0$ ), the front motion is more complex, and in particular, the competition between diffusion and buoyancy effects may lead to a front reversal [8]. On the other hand, when the front is only influenced by Marangoni flows initiated along the free surface, the vertical structure of the flow is different and asymmetric [9]. As a result, even when  $a_0 = b_0$  and  $D_a = D_c = D_b$ , a front reversal of purely Marangoni convective origin can be observed in the course of time, characterized by an initial motion of the front in the direction of the return flow [9]. When the surface tension changes during the reaction are large enough, transient oscillations can also be observed in the presence of Marangoni-driven convection, while sustained oscillations are noted when combined with buoyant forces [10–12]. Recently, as a unique feature of differential diffusion effects coupled with Marangoni stresses, transient spatio-temporal oscillations of surface tension along with a discontinuous motion of the front have been shown to emerge for appropriate conditions on the model parameters, the mechanism of which does not require any autocatalytic feedback nor prescribed hydrodynamic instability [13].

By considering a bimolecular front traveling in the presence of Marangoni-driven convection, we propose here to focus on the role of initial reactants concentrations and of the reaction reversibility on the Marangoni-driven convective front dynamics previously derived for irreversible fronts and for  $a_0 = b_0$  and  $D_a = D_c = D_b$  [9]. The article is organized as follows. In §2, we describe the general model system. In §3, the influence of the ratio of initial reactants concentrations,  $\beta = b_0/a_0$ , on the system dynamics is highlighted. We show that  $\beta = b_0/a_0$  can be used as an experimental control parameter to modulate the speed of the front, the reaction yield and the switching time from the short-time convective regime to the long-time diffusive one. When  $\beta < 1$ , antagonistic effects can also prevent the Marangoni-driven convective front reversal from occurring. Next, we investigate the influence of the backward reaction rate,  $g$ , in §4. We show that, by increasing  $g$ , the front slows down as the gradients of surface tension around the front position become symmetrical, while the surface tension profiles tend to be monotonic. Finally, conclusions and prospects are drawn in §5.

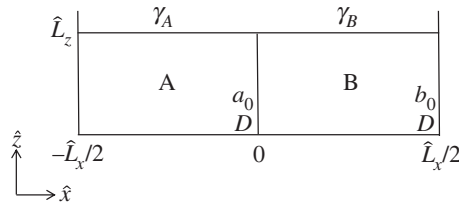


**Figure 1.** Sketch of the system. Two solutions of reactants A and B of concentrations  $a_0$  and  $b_0$  and of surface tension  $\gamma_A$  and  $\gamma_B$ , respectively, are initially separated in space in a two-dimensional domain of length  $\hat{L}_x$  and height  $\hat{L}_z$ . The species diffuse at same rates,  $D$ .

## 2. General model system

We consider a two-dimensional system of length  $\hat{L}_x$  and height  $\hat{L}_z$  open to the air, in which a solution of A of initial concentration  $a_0$  is initially separated from a solution of B of initial concentration  $b_0$  (figure 1). At time  $t > 0$ , A and B meet and react according to the general  $A + B \xrightleftharpoons[k_g]{k_f} C$  reaction scheme, which produces a third species C, with  $k$  the forward rate constant and  $g$  the backward one. The localized reaction zone that forms between the miscible solutions of A and B and in which C is produced is then called the reaction front. All the species diffuse at the same rate  $D$  (assumed constant) and affect the solution surface tension, thereby inducing gradients of surface tension leading to Marangoni-driven flows. We suppose that no evaporation processes occur during the chemical reaction and that the air/liquid interface is not deformable. To focus on surface tension forces, we also take the solution density as constant in space and time preventing any buoyancy-driven convection in solution. The governing equations for this system are therefore obtained by coupling the RDC equations for the concentrations of the reactants  $\hat{a}, \hat{b}$  and of the product  $\hat{c}$  to the two-dimensional incompressible Navier–Stokes equations for the dimensional velocity field  $\hat{\underline{v}} = (\hat{u}, \hat{w})$ . We assume a zero-gravity condition and/or a spatially homogenous solution density. The model reads

$$\frac{\partial \hat{a}}{\partial \hat{t}} + \hat{\underline{v}} \cdot \hat{\nabla} \hat{a} = D \hat{\nabla}^2 \hat{a} - k \hat{a} \hat{b} + g \hat{c}, \quad (2.1)$$

$$\frac{\partial \hat{b}}{\partial \hat{t}} + \hat{\underline{v}} \cdot \hat{\nabla} \hat{b} = D \hat{\nabla}^2 \hat{b} - k \hat{a} \hat{b} + g \hat{c}, \quad (2.2)$$

$$\frac{\partial \hat{c}}{\partial \hat{t}} + \hat{\underline{v}} \cdot \hat{\nabla} \hat{c} = D \hat{\nabla}^2 \hat{c} + k \hat{a} \hat{b} - g \hat{c}, \quad (2.3)$$

$$\frac{\partial \hat{\underline{v}}}{\partial \hat{t}} + (\hat{\underline{v}} \cdot \hat{\nabla}) \hat{\underline{v}} = \nu \hat{\nabla}^2 \hat{\underline{v}} - \frac{1}{\rho_0} \hat{\nabla} \hat{p} \quad (2.4)$$

and  $\text{div} \hat{\underline{v}} = 0, \quad (2.5)$

or, in dimensionless form,

$$\frac{\partial a}{\partial t} + \underline{v} \cdot \nabla a = \nabla^2 a - ab + \bar{g}c, \quad (2.6)$$

$$\frac{\partial b}{\partial t} + \underline{v} \cdot \nabla b = \nabla^2 b - ab + \bar{g}c, \quad (2.7)$$

$$\frac{\partial c}{\partial t} + \underline{v} \cdot \nabla c = \nabla^2 c + ab - \bar{g}c, \quad (2.8)$$

$$\frac{\partial \underline{v}}{\partial t} + (\underline{v} \cdot \nabla) \underline{v} = S_c (\nabla^2 \underline{v} - \nabla p) \quad (2.9)$$

and  $\text{div} \underline{v} = 0, \quad (2.10)$

where  $\bar{g} = g/(ka_0)$  is the dimensionless backward rate constant, and where  $S_c = (\nu/D)$  is the Schmidt number (fixed to  $10^3$  as typical for small species at room temperature in water), with  $\nu = (\mu/\rho_0)$  the kinematic viscosity,  $\mu$  the dynamic viscosity (assumed constant) and  $\rho_0$  the solution density. The problem is made dimensionless by using the characteristic scales of the RD system [9]: for time,  $\tau_c = (1/ka_0)$ , length  $L_c = \sqrt{D\tau_c}$ , velocity  $U_c = (L_c/\tau_c) = \sqrt{D/\tau_c}$  and concentration  $a_0$ . The dimensional dynamic pressure  $\hat{p}$  is rescaled by  $p_c = (\mu/\tau_c) = \rho_0 S_c D/\tau_c$ .

The dimensionless initial conditions are separated reactants such that:

$$a = 1, b = 0, c = 0, \quad \forall z, x < 0 \quad (2.11)$$

and

$$a = 0, b = \beta, c = 0, \quad \forall z, x \geq 0, \quad (2.12)$$

where  $\beta = b_0/a_0$  is the ratio of initial reactant concentrations.

For the boundary conditions (BCs) of figure 1, we use no-flux BCs for the chemical concentrations at each boundary of the domain. The BCs for the fluid velocity field at the rigid boundaries ( $\hat{x} = \pm \hat{L}_x/2$  and  $\hat{z} = 0$ ) are no-slip conditions,  $\hat{u} = 0 = \hat{w}$ . At the free surface, we assume  $\hat{w} = 0$ , and we use a Marangoni BC for  $\hat{u}$  derived from the tangential stress balance condition of the form,  $\mu(\partial\hat{u}/\partial\hat{z}) = \partial\hat{\gamma}/\partial\hat{x}$  at the free surface [14,15], or in a dimensionless form,

$$\frac{\partial u}{\partial z} = - \sum_i M_i \frac{\partial c_i}{\partial x} \quad \text{at } z = L_z, \quad (2.13)$$

where  $L_x$  and  $L_z$  represent the dimensionless length and height of the system, respectively. In equation (2.13), the dimensionless solutal Marangoni number  $M_i$  of species  $i = (a, b, c)$ , which quantifies the influence of each chemical species on the solution surface tension, is defined as follows:

$$M_i = - \frac{1}{\mu} \sqrt{\frac{a_0}{Dk}} \frac{\partial \hat{\gamma}}{\partial \hat{c}_i}, \quad (2.14)$$

where  $\hat{\gamma}$  and  $\hat{c}_i$  are the dimensional solution surface tension and concentration of solute  $i$ , respectively.

For sufficiently dilute solutions, we expect the solution surface tension to vary linearly with the concentrations. Then, we can write that  $\hat{\gamma} = \hat{\gamma}_0 + \sum_i (\partial\hat{\gamma}/\partial\hat{c}_i)\hat{c}_i$ , with  $\hat{\gamma}_0$  the (dimensional) surface tension of the solvent ( $\hat{c}_i = 0, \forall i$ ). Using equation (2.14), the dimensionless solution surface tension, which is defined as  $\gamma = (\hat{\gamma} - \hat{\gamma}_0)/\hat{\gamma}_c$ , where  $\hat{\gamma}_c = p_c L_c$ , then reads

$$\gamma(x, t) = -M_a a(x, L_z, t) - M_b b(x, L_z, t) - M_c c(x, L_z, t). \quad (2.15)$$

In equations (2.14) and (2.15), we take  $M_{a,b,c} \geq 0$  to describe surfactants decreasing the surface tension of the solvent, i.e.  $(\partial\hat{\gamma}/\partial\hat{c}_i) < 0, \forall i$ . From equation (2.15), we note that the surface tensions of the initial pure A and B solutions read  $\gamma_A = -M_a$  and  $\gamma_B = -M_b\beta$ , respectively.

Despite its simplicity, the Marangoni BC, equation (2.14), which couples the fluid motion to the RDC dynamics, has been successfully applied in microgravity experiments involving autocatalytic reactions [16]. A similar BC has also been applied to describe the neutralization reaction in immiscible systems when the octanoic (caprylic) acid,  $R\text{-COOH}$  with  $R = \text{CH}_3(\text{CH}_2)_6$ , dissolved in hexane, reacts with sodium hydroxide (NaOH), dissolved in the aqueous phase in a vertically placed Hele–Shaw cell [17]. Similar reactants involved in such acid–base reactions could provide potential candidates for the experimental verification of the presented model. Complexation reactions could also be envisioned [18].

The system dynamics is then obtained by numerically integrating the complete set of equations (2.6)–(2.10) subjected to initial conditions and BCs specified above, with the numerical procedure described in [19]. We consider two particular scenarios. In the next section, we present the dynamics of the reactive flow and of the front by considering  $\bar{g} = 0$  and  $\beta \neq 1$ , so as to highlight the effect of different initial reactants concentrations on the system dynamics. Next, to investigate reversibility effects on the front, we consider  $\beta = 1$  and  $\bar{g} \neq 0$ . In both scenarios, the length  $L_x$  is

chosen sufficiently large so that the results are not affected by lateral boundary effects on the time of interest, typically  $L_x = 200$ .

### 3. Classification of Marangoni-driven nonlinear dynamics for unequal initial concentrations of reactants

In this section, we highlight the effect of initial reactants concentrations on the Marangoni-driven  $A + B \rightarrow C$  convective front dynamics. Throughout the text, we shall summarize the results for  $\beta = 1$  and we refer the readers to [9] for additional details.

When  $\beta = 1$ , we have shown that the surface tension profiles can be reconstructed from a one-dimensional RD analysis based on the conservation law,  $(a + b + 2c) = 1 \forall(x, t)$  [9]. When  $\beta \neq 1$ , this conservation law is broken, and thus, a similar analysis cannot be used. Fortunately, on the basis of the long-time asymptotic analysis of Trevelyan *et al.* [20], one can still predict the monotonic properties of RD profiles when  $\beta \neq 1$  (see [20] for the analytical derivation of the corresponding RD profiles, along with the change of notation  $\rho \leftrightarrow -\gamma$ ) (figure 2a). The classification then obtained generalizes for all values of  $\beta$ , the classification proposed in [9] for  $\beta = 1$  and is presented in figure 2a.

In figure 2a, the shaded regions (including the diagonal and vertical dotted lines) are the regions of monotonic surface tension profiles driving a single convective roll. This single convective roll is deduced from the simplest idea that the flow is initiated along the air–liquid interface from the lowest surface tension region to the largest one and that a return flow emerges in the bulk liquid phase due to the incompressibility condition. Outside the shaded regions, the profiles are nonmonotonic with a maximum when  $M_c < (1 + \beta^{-1})M_a$  and a minimum when  $M_c > (1 + \beta^{-1})M_a$ . The same analysis than mentioned earlier for the flow structure leads to two counterclockwise convective rolls. At the solid line of figure 2a, when  $M_b = \beta^{-1}M_a$ , the profiles are nonmonotonic (two convective rolls), except when  $M_c = (1 + \beta^{-1})M_a$  or  $M_c = (\beta + 1)M_b$  (intersection between the dotted and solid lines in figure 2a), for which the surface tension is spatially constant for all times and thus where we expect no flow. In the presence of convection, we numerically verify such a classification. We illustrate this for the surface tension profiles when  $\beta = 0.5$  in figure 2b. The profiles corresponding to the separating lines (dotted and solid lines) of figure 2a are also illustrated with convection in figure 2c. Since the chemo-hydrodynamic patterns resemble those found for  $\beta = 1$  [9], we only show the typical structure of the flows and of the chemical front in figure 3, for region I.

A quantity that is of particular interest is the reaction yield, which is proportional to the total amount of C produced,  $c_{\text{tot}} = \int_0^{L_x} \int_0^{L_z} c(x, z, t) dx dz$ , for a given amount of (limiting) reactants consumed. Independently of  $\beta$ , we note that the mixing driven by convection and diffusion increase the total amount of C produced (and hence, the reaction yield) with respect to when there is no flow (RD), i.e.  $c_{\text{tot}}(t) > c_{\text{tot}}(t) \text{ (RD)}$ ,  $\forall t$  and for all the values of  $\beta$  tested. This is illustrated for some values of  $\beta$  in figure 4a. Moreover, when increasing  $\beta$ , the difference of the total amount of C produced with and without flow becomes more important (figure 4b). Such results highlight the potential use of Marangoni-driven convection as an efficient mixing technique to enhance reaction yields.

We next turn our attention to the effect of  $\beta$  on the propagation of the chemical front. In the absence of convection, when  $\beta \neq 1$ , diffusion drives a motion of the front in the direction of the smallest concentration side or equivalently, of the smallest diffusive flux. Thus, when  $\beta > 1$ , the front propagates to the left (towards the A-side), and the opposite when  $\beta < 1$  [1]. When convection is present, we can therefore expect antagonistic effects on the front propagation between such a diffusion-driven propagation and the convection-driven one as detailed in [9] and summarized later. We now review the effect of  $\beta$  at fixed liquid depth  $L_z$  on the RDC front dynamics. We restrict the analysis to each region of the upper part of figure 2a (above and on the solid line, i.e.  $M_b \beta \geq M_a$ ), with no loss of generality. The lower part can be deduced straightforwardly.

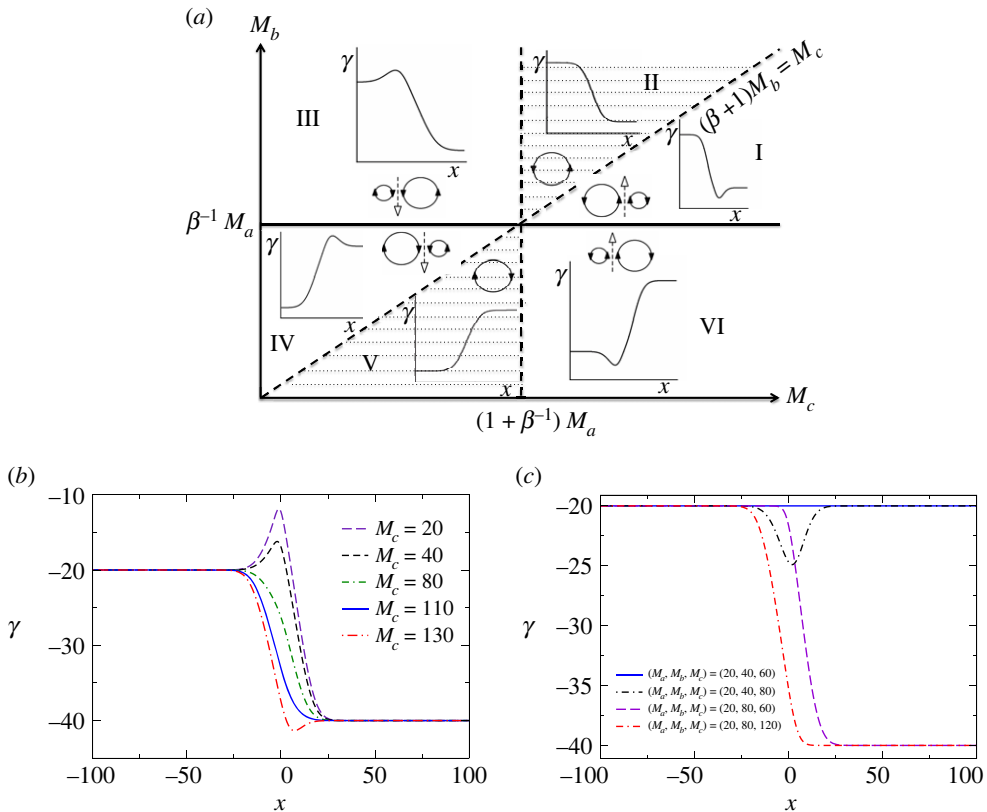


**Figure 2.** (a) Sketch of the RD surface tension profiles and expected convective rolls in the  $(M_b, M_c)$  plane at fixed  $M_a$  for arbitrary ratio of initial concentrations of reactants,  $\beta$ . This scheme generalizes the classification provided for  $\beta = 1$  in [9] and holds in the presence of convection. (b) Numerical surface tension profiles along  $x$  at  $t = 30$  when  $\beta = 0.50$ ,  $L_z = 5$  and for  $M_a = 20$ ,  $M_b = 80$  and different values of  $M_c$ ,  $M_c = 20, 40, 80, 110, 130$ , from top to bottom. Notice that the solution surface tension changes from  $-M_a$  to  $-M_b\beta$  from the pure A- to the pure B-sides, respectively. (c) Corresponding surface tension profiles for  $L_z = 5$ ,  $\beta = 0.50$  at  $t = 30$  when  $(M_a, M_b, M_c) = (20, 80, 60), (20, 40, 80), (20, 80, 120), (20, 40, 60)$ , corresponding to the vertical, horizontal, diagonal lines as well as the intersection of the solid and dotted lines of (a), respectively. (Online version in colour.)

We recall that the front position  $x_f$  is here defined as the point where the depth-averaged production rate  $\langle ab \rangle$  reaches its maximum [9]. Depth-averaged quantities are all defined as  $\langle \phi \rangle(x, t) = (1/L_z) \int_0^{L_z} \phi(x, z, t) dz$ , where  $\phi$  stands for the considered scalar field ( $a, b, c$  or  $ab$ ).

In region I of figure 2a (two convective rolls), when  $\beta = 1$ , the front is driven in the direction of the weakest flow (smallest surface tension gradient) [9], i.e. in the right direction ( $x_f > 0$ , see solid line in figure 5a). Indeed, the front is mainly located in the bulk (at the convergence points between the two convective rolls) and is pushed stronger to the right by the biggest convective roll than to the left by the smallest one. When  $\beta < 1$ , diffusive and convective effects make the front propagate in the right direction, where both the surface tension gradient and diffusive flux of reactants are the smallest and the flow is the weakest (figure 5a). By decreasing  $\beta$ , the front propagates faster in the long-time diffusive limit because of larger diffusive fluxes. We note the opposite in the short-time convective regime where convective effects on the front position weaken as the asymmetry between the two convective rolls decreases, i.e.  $M_b\beta$  converges to  $M_a$  in region I as  $\beta$  decreases. When  $\beta > 1$ , antagonistic effects occur. As for  $\beta = 1$ , we recover that the front initially propagates in the direction of the weakest flow (to the right), while the diffusion-driven propagation takes over only for longer times (figure 5b). By increasing  $\beta$ , the asymmetry between the two convective

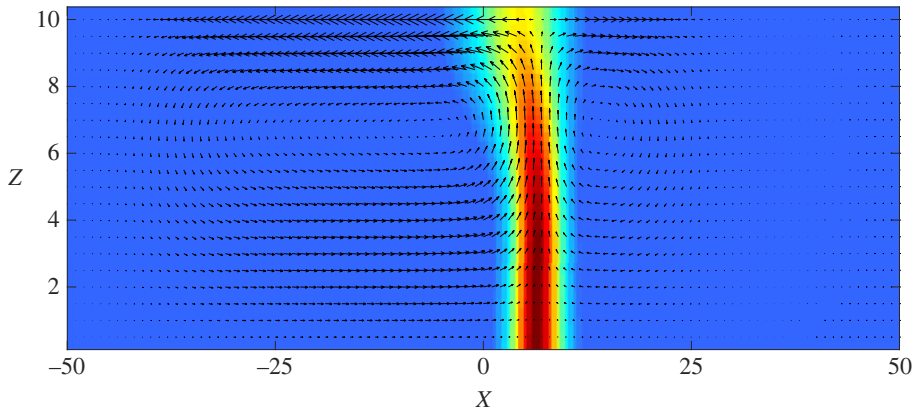


**Figure 3.** Focus on the convective rolls centred on the deformed reaction front at  $t = 30$  for  $L_z = 10$ ,  $(M_a, M_b, M_c) = (20, 80, 150)$  and  $\beta = 0.5$  (region I in figure 2a). The fluid velocity field is superimposed on a two-dimensional plot of the production rate, which ranges between its maximum value shown in red, and its minimum value,  $ab_{\min} = 0$ , shown in blue. The  $z$ -direction has been magnified to see the details of the velocity field. The velocity vectors are here tripled compared to their effective length to allow for a better visualization. (Online version in colour.)

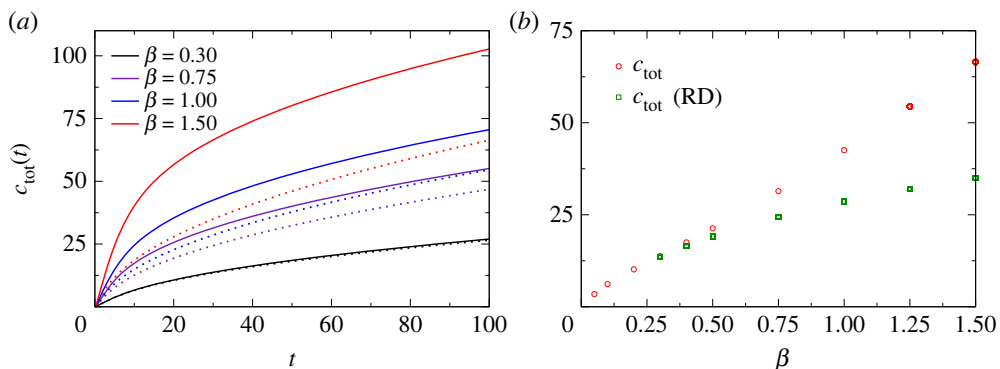


**Figure 4.** Total amount of species C produced when  $M_a = 20$ ,  $M_b = 80$  and  $M_c = 150$  for  $L_z = 5$  (a) in the course of time and (b) at a particular time  $t = 30$ . (a) The temporal evolution of  $c_{\text{tot}}$  is plotted for  $\beta = 0.30, 0.75, 1, 1.50$  from bottom to top. The dotted lines are the corresponding RD solutions (in the same order with respect to  $\beta$ ). By increasing  $\beta$ ,  $c_{\text{tot}}(t) > c_{\text{tot}}(t)$  (RD),  $\forall t$ . (b) Increasing  $\beta$  enlarges the difference with the corresponding RD solution. (Online version in colour.)

rolls increases and the front travels faster in the direction of the weakest flow. Since the diffusive flux of B also increases with  $\beta$ , the front also travels faster in the long-time limit but in the opposite direction (figure 5b). Moreover, increasing  $\beta$  also decreases the switching time from the short-time convective regime to the long-time diffusive one. Similar conclusions can be deduced for region III. In that region, the front position is along the free surface, as for  $\beta = 1$  (see [9] for more details).

We can corroborate those quantitative effects of  $\beta$  on the system dynamics from a small-time asymptotic analysis of the RDC equations, equations (2.6)–(2.8) with  $\bar{g} = 0$ . We first rescale the equations with respect to  $\beta$ , by introducing the rescaled variable,  $\bar{b} = b/\beta$ . Equations (2.6)–(2.8) then write, respectively,  $\partial_t a + \underline{v} \cdot \nabla a = \nabla^2 a - a\bar{b}\beta$ ,  $\partial_t \bar{b} + \underline{v} \cdot \nabla \bar{b} = \nabla^2 \bar{b} - a\bar{b}$ , and  $\partial_t c + \underline{v} \cdot \nabla c = \nabla^2 c + a\bar{b}\beta$ . The initial condition becomes  $(a, \bar{b}) = (1, 0)$  and  $(a, \bar{b}) = (0, 1) \forall z$ , for  $x < 0$  and  $x \geq 0$ , respectively. The BCs are unchanged, except for the Marangoni BC, equation (2.13), that becomes  $\partial_z u = -M_a \partial_x a - \beta M_b \partial_x \bar{b} - M_c \partial_x c$ . In the short-time asymptotic limit ( $t \rightarrow 0$ ),  $c \rightarrow 0$ , and thus from the equation of  $c$ ,  $a\bar{b}\beta \rightarrow 0$ . Then, in the short-time limit, the leading-order equations for  $a$

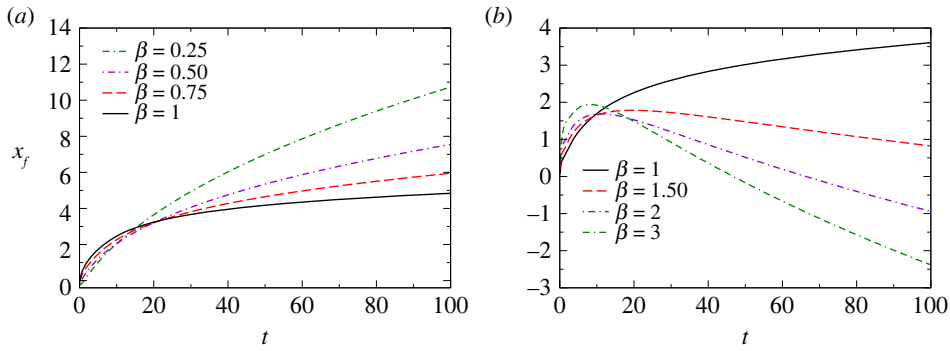


**Figure 5.** Front trajectories,  $x_f(t)$  for region I of figure 2a for (a)  $\beta \leq 1$  and (b)  $\beta \geq 1$ . The model parameters are  $L_2 = 5$  and (a)  $(M_a, M_b, M_c) = (20, 80, 150)$  and (b)  $(M_a, M_b, M_c) = (20, 80, 400)$ . (a) The front propagates to the right for all times. (b) Antagonistic effects make the front reverse its direction of propagation in the course of time. Independently of the considered Marangoni numbers in region I, the dynamics of the front is dominated by diffusive effects in the long-time limit, i.e.  $x_f < 0$  ( $x_f > 0$ ) when  $\beta > 1$  ( $\beta < 1$ ). (Online version in colour.)

and  $b$  are the corresponding transport (diffusion and convection) equations, while the leading-order Marangoni BC is  $\partial_z u = -M_a \partial_x a - \beta M_b \partial_x \bar{b}$ . Hence, in this limit, increasing  $\beta$  at fixed  $M_b$  is equivalent to increasing  $M_b$  at fixed  $\beta$ , which therefore strengthens convective motions and increases the asymmetry between the two convective rolls (i.e. the ratio  $M_b \beta / M_a$  increases). Thus, convective effects on the front dynamics are enhanced and the front speeds up. As time evolves, the concentration of species C becomes non-negligible and the reaction term ( $\beta a \bar{b}$ ) becomes important. In this case, from the RDC equations of  $a$  and  $c$ , we note that  $\beta$  plays the additional role of a (dimensionless) reactive time scale for the consumption and production of species A and C, respectively. Hence, the switching time from the short-time convective regime to the long-time diffusion limit is expected to be controlled by  $\beta$  as numerically observed.

Eventually, we comment on the case,  $M_a = M_b \beta$  (solid line of figure 2a). For  $\beta = 1$ , the two convective rolls are symmetrical (identical size and intensity) leading to a steady front ( $x_f = 0$ ) for all times [9]. When  $\beta \neq 1$ , convection superimposes on an already moving RD front, and such a symmetry is broken. In this case, convective effects on the front dynamics are negligible, and we can consider that the front moves in the direction of smallest diffusive flux for all times, i.e.  $x_f(t) < 0$  when  $\beta > 1 \forall t$ , and vice versa (figure 6).

In region II of figure 2a (one convective roll), when  $\beta = 1$ , the front initially propagates in the direction of the return flow (right side) and a front reversal of purely convective origin occurs when  $M_c < M_a + M_b$  for intermediate times [9] (see solid line in figure 7a). When  $\beta < 1$ , the diffusion-driven propagation (to the right) can prevent the front reversal from showing up (figure 7a). For any considered value of  $M_c < M_a + M_b$ , we find that, when  $\beta < \beta_{\min}^{\text{II}}$ , where  $\beta_{\min}^{\text{II}}$  is a function of the considered model parameters, the front dynamics is observed to be dominated by diffusive processes and the front reversal is prevented. The stronger the convective motions, the smaller the value of  $\beta$  for diffusion to take over (i.e. the smaller  $\beta_{\min}^{\text{II}}$ ). In particular,  $\beta_{\min}^{\text{II}}$  decreases with increasing  $L_2$  or with increasing all the Marangoni numbers (see dotted lines in figure 7a). In the opposite case ( $\beta > \beta_{\min}^{\text{II}}$ ), however, a double switch of direction of the front is noted. When  $\beta \geq 1$ , the front initially travels in the direction of the return flow while moving in the opposite direction in the long-time diffusive limit (figure 7b). In this case, the convective front reversal is enhanced by increasing  $\beta$  since the convective roll intensifies with  $M_b \beta$ . Hence, for the model parameters tested in region II, the convective dynamics observed for  $\beta = 1$  is recovered when  $M_c \geq M_a + M_b$ , and when  $M_c < M_a + M_b$ , except when  $\beta < \beta_{\min}^{\text{II}} < 1$  for which the diffusion-driven motion of the front takes over on the convective front reversal dynamics. We note that the condition  $M_b \beta > M_a$  (that applies for regions I, II and III of figure 2a) ensures that

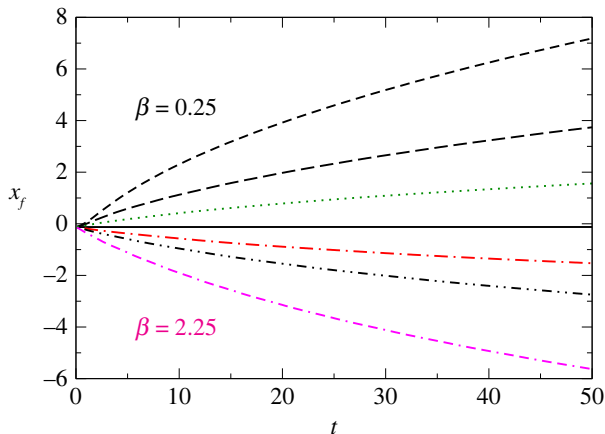


**Figure 6.** Front trajectories,  $x_f(t)$ , for parameters on the solid line of figure 2a, for various values of  $\beta$ , with  $L_z = 5$ ,  $M_a = 20$  and  $M_b = M_a/\beta$ . From top to bottom,  $\beta = 0.25, 0.50, 0.75, 1, 1.25, 2, 2.25$ . When  $\beta = 1$  (black solid line), the front is steady for all times. When  $\beta \neq 1$ , the front propagates in the direction of the smallest diffusive flux for all times, i.e.  $x_f(t) < 0$ , when  $\beta > 1$  and vice versa,  $\forall t$ . (Online version in colour.)

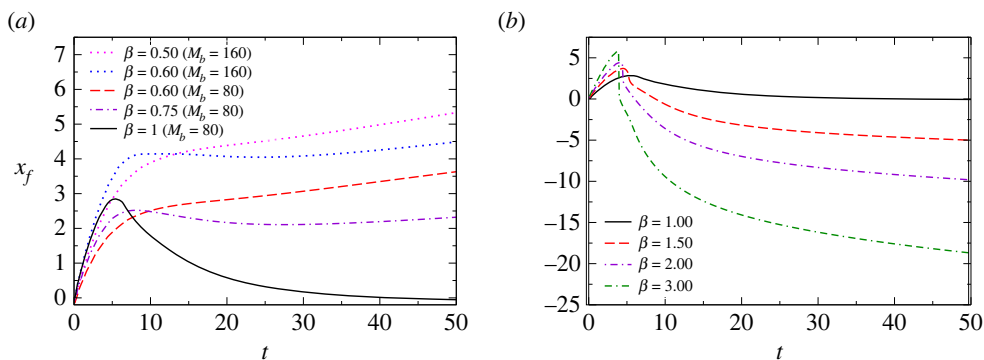


**Figure 7.** Front trajectories,  $x_f(t)$  for region II of figure 2a for (a)  $\beta \leq 1$  and (b)  $\beta \geq 1$ . (a)  $L_z = 5$  and we consider two sets of Marangoni numbers,  $(M_a, M_b, M_c) = (20, 80, 80)$  and  $(M_a, M_b, M_c) = 2 \times (20, 80, 80) \equiv (40, 160, 160)$  (dotted lines). The front reversal is prevented below a critical value of  $\beta$ ,  $\beta_{\min}^{\text{II}} = 0.68 \pm 0.08$  for  $(M_a, M_b, M_c) = (20, 80, 80)$  and  $\beta_{\min}^{\text{II}} = 0.55 \pm 0.05$  for  $(M_a, M_b, M_c) = (40, 160, 160)$ . (b)  $L_z = 5$  and  $(M_a, M_b, M_c) = (20, 80, 80)$ . The front reversal is enhanced by increasing  $\beta$ . Independently of the considered Marangoni numbers in region II, in the long-time limit, the dynamics of the front is dominated by diffusive effects, i.e.  $x_f < 0$  when  $\beta > 1$  and vice versa. (Online version in colour.)

the line  $M_c = M_a + M_b$  is always located in between the boundary lines  $M_c = (1 + \beta^{-1})M_a$  and  $M_c = (\beta + 1)M_b$  that enclose region II in figure 2a, i.e.  $(1 + \beta^{-1})M_a < (M_a + M_b) < (\beta + 1)M_b$ .

#### 4. Reaction reversibility effects

Here, we extend the analysis of the Marangoni-driven dynamics to bimolecular  $A + B \xrightleftharpoons[k]{k} C$  reversible fronts, with  $k$  and  $g$  being the forward and backward rate constants, respectively. To highlight the effect that reversibility can have on the convective frontal dynamics, we focus hereafter on the case  $\beta = 1$ . Except for the direction of front propagation, the main conclusions of this part, however, do not depend on  $\beta$ .

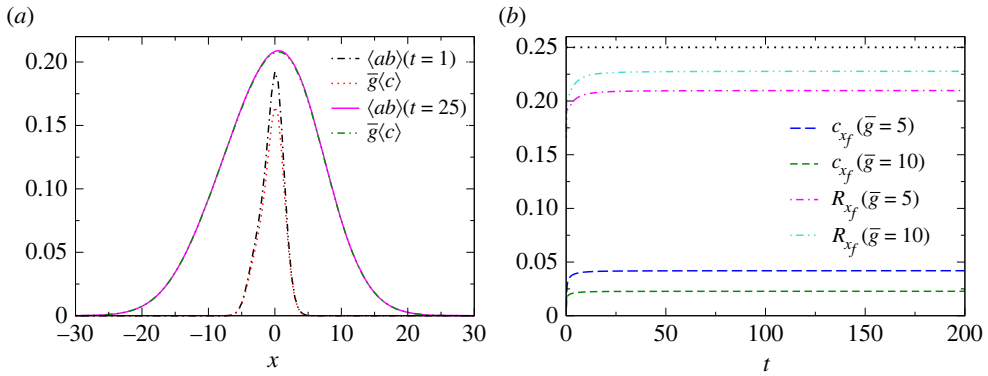


**Figure 8.** (a) Depth-averaged forward and backward reaction rates, respectively, noted  $\langle ab \rangle(x, t)$  and  $\bar{g}\langle c \rangle(x, t)$ , at different times for  $\bar{g} = 5$ . (b) Local reaction rate,  $R_{x_f}(t) = \langle ab \rangle(x = x_f, t)$ , and concentration of C at the front position,  $c_{x_f} = \langle c \rangle(x = x_f, t)$ , as a function of time for different values of  $\bar{g}$ . The dotted line denotes the maximum possible value of  $R_{x_f} = 1/4$ . At fixed  $\bar{g}$ ,  $ab$  converges to  $\bar{g}c$  in the long-time limit ( $t \gg 1/\bar{g}$ ). In this limit,  $R_{x_f}$  and  $c_{x_f}$  reach steady values. (a,b) The model parameters are  $M_a = 20, M_b = 40$  and  $M_c = 150$  when  $L_z = 5$ . (Online version in colour.)

In the pure reversible RD case, a domain of local equilibrium is reached in the long-time limit in the reaction zone where the reaction rates balance each other, i.e. in dimensionless variables, where  $ab = \bar{g}c$  [2]. In the presence of convection and by averaging along the depth, we recover this balance of reaction rates  $\langle ab \rangle = \bar{g}\langle c \rangle \forall x$ , for large times ( $t \gg 1/\bar{g}$ ) (figure 8a). Since the reversible regime starts to play a significant role for times  $t > 1/\bar{g}$ , the larger  $\bar{g}$ , the faster the convergence to the reversible regime. In particular, in the limit  $\bar{g} \rightarrow \infty$ , the reversible regime dominates the system dynamics for all times, so that  $ab \rightarrow \bar{g}c \forall (x, z, t)$ , and equations (2.1)–(2.3) reduce to the corresponding transport equations.

Due to the local equilibrium, we note that the local production rate of C,  $R_{x_f}$ , and the maximum of the concentration of C at the reaction zone position,  $c_{x_f}$ , reach steady values (figure 8b). The maximum of  $R_{x_f}$  is obtained when the concentration of C is zero, i.e. when  $a + b = 1$  or when  $a = 1/2 = b$ . Hence, the steady value of  $R_{x_f}$  is bounded superiorly by  $1/4$  (see dotted line in figure 8b). Note that, however, the components of the fluid velocity field do not converge to steady values since the gradients of surface tension always evolve with time.

We next focus on the effects of reversibility on the monotonic properties of surface tension profiles. For times  $t \ll 1/\bar{g}$ , the profiles follow the predictions from the irreversible regime (figure 2a). As time evolves, the backward reaction plays a role and converts back the product into the reactants with the effect to reduce the concentration of C inside the reaction zone. Hence, species C affects less the surface tension, and the extremum formed in the profiles of surface tension is less pronounced with respect to the pure irreversible case (figure 9a). Thus, we find the existence of a maximum value of  $\bar{g}$  ( $\bar{g}_{\max}$ ) for the classification of figure 2a to remain valid or equivalently, above which the profiles of surface tension are monotonic independently of the zone considered in figure 2a (figure 9a). Such a critical value is a non-universal function of the model parameters that, in particular, increases with increasing  $M_c$  (figure 9b). Below, we corroborate this observation analytically.

Firstly, we show that the surface tension profiles must be monotonic profiles in the limit,  $\bar{g} \rightarrow \infty, \forall t$ . Indeed, by summing equations (2.1) + (2.2) +  $2 \times$  (2.3), we find the conservation law,  $a + b + 2c = 1 \forall (x, z, t)$ , since  $\beta = 1$ . In particular, in the limit  $\bar{g} \rightarrow \infty, c \rightarrow 0$ , and this law reduces to  $a + b = 1 \forall (x, z, t)$ . Thus, the gradient of surface tension writes  $\partial_x \gamma = -M_a \partial_x a - M_b \partial_x b = (M_a - M_b) \partial_x b$ . Since  $\partial_x b \geq 0$  is single-signed,  $\partial_x \gamma$  is also single-signed and writes  $\partial_x \gamma \leq 0$  when  $M_b > M_a$  (monotonic decreasing) and  $\partial_x \gamma \geq 0$  when  $M_b < M_a$  (monotonic increasing). On the other hand, in the limit  $\bar{g} \rightarrow 0$ , we must recover the classification as provided in figure 2a (with  $\beta = 1$ ). Thus, we infer the existence of a critical value,  $\bar{g}_{\max}$ , above which the profiles are monotonic.

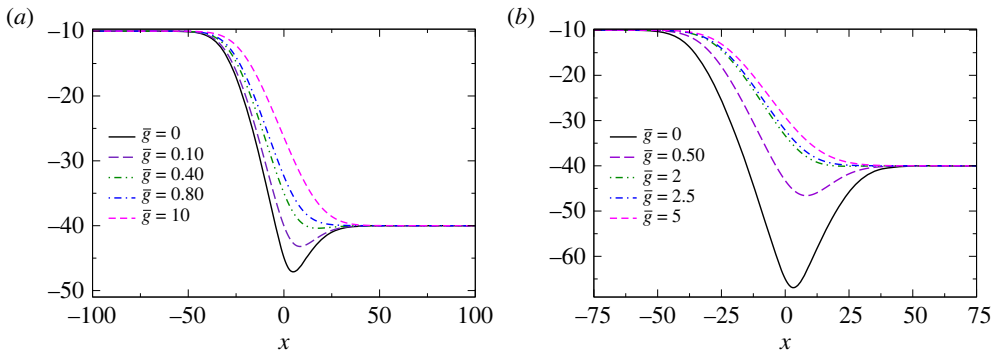


**Figure 9.** Numerical surface tension profiles along  $x$  for different values of the backward rate constant,  $\bar{g}$ , at  $t = 100$  for  $M_a = 10, M_b = 40$  and (a)  $M_c = 100$  and (b)  $M_c = 150$ . When  $\bar{g} > \bar{g}_{\max}$ , the large-time surface tension profiles are monotonic. In particular, (a)  $\bar{g}_{\max} = 0.60 (\pm 0.20)$  and (b)  $\bar{g}_{\max} = 2.25 (\pm 0.25)$ . (Online version in colour.)

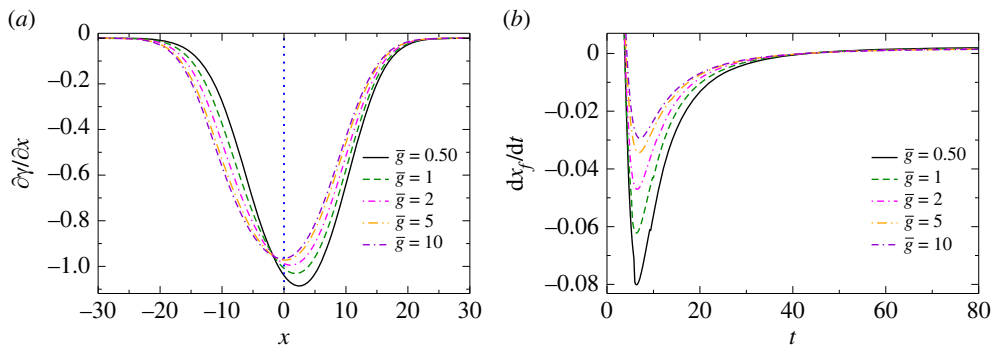


**Figure 10.** (a) Profiles of surface tension gradients  $\partial\gamma/\partial x$  and (b) speed of the front  $dx_f(t)/dt$  for various values of the backward rate constant,  $\bar{g}$ . The model parameters are  $M_a = 20, M_b = 40$  and  $M_c = 2M_a$  (vertical line of figure 2a with  $\beta = 1$ ). (a,b) The asymmetry of the surface tension gradient is less pronounced with respect to the symmetry axis of the system ( $x = 0$ ) and  $dx_f(t)/dt$  decreases (in absolute value) when increasing  $\bar{g}$ . (Online version in colour.)

When  $\bar{g} > \bar{g}_{\max}$ , the structure of Marangoni-driven flows is simplified and corresponds either to a clockwise convective roll when  $M_b < M_a$  or to a counterclockwise convective roll when  $M_b > M_a$  [9].

By increasing  $\bar{g}$ , the diffusive fluxes of reactants across the reaction zone tend to equalize. In particular, in the limit  $\bar{g} \rightarrow \infty$ , since  $a + b = 1 \forall(x, t)$ , we deduce that  $\partial_x a = -\partial_x b \forall(x, t)$ , and thus, the fluxes (or gradients) are symmetrical with respect to the symmetry axis ( $x = 0$ ). This means that the gradient of surface tension is also symmetrical with respect to the same axis since  $\partial_x \gamma = (M_a - M_b) \partial_x b$  (figure 10a). Hence, reaction reversibility affects the propagation of the front and in particular slows down the front. Then, the front speed decreases in the reversible regime with increasing  $\bar{g}$  (figure 10b). Even in the presence of symmetrical diffusive fluxes of reactants, the front does not reach a steady state due to the presence of Marangoni-driven flows. We note that such flows conduct the front in the direction of the return flow (i.e. to the right for a counterclockwise convective roll, see §3) for large times in the reversible regime, i.e.  $dx_f(t)/dt \geq 0$ , as  $t \rightarrow \infty, \forall g$  (figure 10b).

The long-time scalings ( $t \gg 1/\bar{g}$ ) with time of the front properties of the reversible problem are governed by transport processes. For large times, when convective effects are negligible, such time scalings are dominated by diffusion, and the related exponents asymptotically converge to those predicted from the related RD model [2]. However, before reaching such a long-time

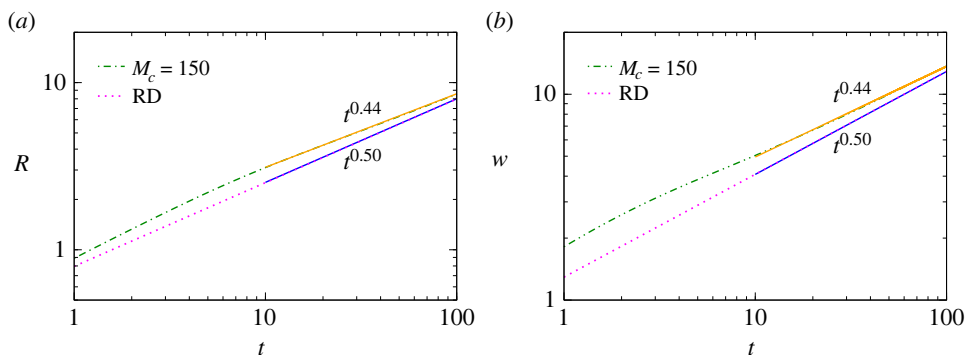


**Figure 11.** (a) Temporal evolution of global reaction rate,  $R(t)$ , and (b) reaction width  $w(t)$ , when  $L_z = 5$  and  $M_a = 20$ ,  $M_b = 40$  and  $M_c = 150$  (log scales). For the sake of comparison, the RD solutions are added (dotted lines). The numerical data are fitted by scaling laws (solid lines) of the forms,  $R \sim t^\mu$  and  $w \sim t^\nu$ , within the time interval of  $t = 10$  and  $t = 100$ . We note that the exponents differ from RD predictions, i.e.  $(\nu, \mu) < 1/2$ . (Online version in colour.)

limit, discrepancies might be found. We illustrate such discrepancies for the reaction width  $w \sim t^\nu$  and global rate  $R \sim t^\mu$ . The latter is defined as  $R = \int_0^{L_x} \langle ab \rangle(x, t) dx$ , while the former is defined as [1] through the second moment of the depth-averaged reaction rate  $\langle ab \rangle(x, t)$ , i.e.  $w^2(t) = \int_0^{L_x} (x - x_f)^2 \langle ab \rangle(x, t) dx / \int_0^{L_x} \langle ab \rangle(x, t) dx$ . In the regime of time considered, we recover  $\nu = 1/2 = \mu$  for the RD front while we find sub-diffusive time scalings, i.e.  $(\nu, \mu) < 1/2$ , with convection (figure 11).

## 5. Conclusion

By initially separating the reactants of a bimolecular reaction, a chemical front can be formed and propagates in the presence of Marangoni flows when gradients of surface tension develop across the reaction zone. The dynamics of such a zone is then described by reaction, diffusion and Marangoni-driven convection processes that we have analyzed both numerically and analytically for equal diffusion coefficients of all species.

We have generalized the results of the Marangoni-driven  $A + B \rightarrow C$  front dynamics initially derived for equal initial concentrations of reactants ( $\beta = 1$ , where  $\beta = b_0/a_0$ ) to arbitrary values of  $\beta$ . As for  $\beta = 1$ , we found two types of surface tension profiles, either monotonic or nonmonotonic with a single extremum, that we have classified as a function of the Marangoni numbers valid for arbitrary  $\beta$  (figure 2a). The structure of chemically driven Marangoni convection is then similar to  $\beta = 1$ , and in particular, a maximum number of two convective rolls can be observed in solution. Since convection superimposes on an already moving RD front when  $\beta \neq 1$ , there are no symmetric profiles, and the front moves even for  $M_a = M_b\beta$ . The role of  $\beta$  on the Marangoni-driven convective front dynamics is highlighted. As for  $\beta = 1$ , we found that the front is initially driven in the direction of weakest flow (smallest surface tension gradient) in regions I and III. Further, varying  $\beta$  affects the speed of the front (increasing it with increasing  $\beta$  in the short-time convective regime) and the switching time from the short to the long-time diffusive regime decreases with increasing  $\beta > 1$  or decreasing  $\beta < 1$  in the upper part of figure 2a. For the specific case where  $M_a \simeq M_b\beta$ , diffusive effects can be considered to dominate the front dynamics for all times. In region II, we showed that the convective front reversal previously observed for  $\beta = 1$  in [9] is prevented if  $\beta < 1$ , when  $\beta$  is below a minimum value function of the model parameters (i.e.  $\beta < \beta_{\min}^{\text{II}}$ ).

When reaction reversibility is included in the analysis, in the form of  $A + B \xrightleftharpoons[k]{g} C$  chemical fronts, a local equilibrium state is reached inside the reaction zone in the reversible regime

( $t \gg 1/\bar{g}$ , where  $\bar{g} = g/k$ ), where the forward and backward reaction rates balance each other. By increasing  $\bar{g}$ , the amount of product inside the reaction zone and hence the amplitude of the extremum formed in the surface tension profiles decrease. In particular, above a maximum value for  $\bar{g}$  (i.e.  $\bar{g} > \bar{g}_{\max}$ ), the profiles are monotonic in the reversible regime leading to a single convective roll, independently of the considered Marangoni numbers. Since reversibility reduces the asymmetry between the diffusive fluxes of reactants, the front is also observed to propagate more slowly in the reversible regime. Also, we quantified discrepancies with predictions based on the related RD reversible model in the intermediate time regime when Marangoni-driven convective effects are observed to be important.

As a natural extension of this work, we could investigate differential diffusion effects on the system dynamics, starting with the case  $a_0\sqrt{D_a} = b_0\sqrt{D_b}$ , where the RD front is stationary, since it is naturally more common in experiments that species diffuse at different rates. On the basis of the recent findings that differential diffusion effects coupled with Marangoni stresses can trigger spatio-temporal oscillations of surface tension along with a discontinuous motion of the front along the free surface [13], we expect much more exotic possibilities for the dynamical properties of the reaction front when all the species diffuse at different rates. Along the same line, the effects of reaction exothermicity in both cases of cooperative and competitive solutal and thermal effects and the coupling to buoyancy-driven convection for unequal initial reactants concentrations and/or differential diffusion effects could be envisioned. Also, the role of adsorption of surface-active species on the dynamics could next be taken into account through the coupling of interface equations to bulk equations. Last but not least, we hope for more experimental works to be undertaken in the future to check all such theoretical findings of convective effects on frontal chemical systems.

**Data accessibility.** This article has no additional data.

**Authors' contributions.** R.T.: formal analysis, writing—original draft and writing—review and editing; L.R.: supervision and validation, review and editing.

All authors gave final approval for publication and agreed to be held accountable for the work performed therein.

**Conflict of interest declaration.** We declare we have no competing interests.

**Funding.** The authors thank the 'Actions de Recherches Concertées' program and the F.R.S.-FNRS for their financial support.

## References

- Gálfi L, Rácz Z. 1988 Properties of the reaction front in an  $A + B \rightarrow C$  type reaction-diffusion process. *Phys. Rev. A* **38**, 3151–3154. (doi:10.1103/PhysRevA.38.3151)
- Chopard B, Droz M, Karapiperis T, Rácz Z. 1993 Properties of the reaction front in a reversible  $A + B \xrightleftharpoons[k]{g} C$  reaction-diffusion process. *Phys. Rev. E* **47**, R40–R43. (doi:10.1103/PhysRevE.47.R40)
- Kostarev KG, Shmyrov AV, Zuev AL, Viviani A. 2011 Convective and diffusive surfactant transfer in multiphase liquid systems. *Exp. Fluids* **51**, 457–470. (doi:10.1007/s00348-011-1063-9)
- Schwarzenberger K, Aland S, Domnick H, Odenbach S, Eckert K. 2015 Relaxation oscillations of solutal Marangoni convection at curved interfaces. *Colloids Surf. A Physicochem. Eng. Asp.* **481**, 633–643. (doi:10.1016/j.colsurfa.2015.06.031)
- Kostarev K, Denisova M, Shmyrov A. 2018 Effect of Marangoni convection on surfactant transfer between the drop connected to the reservoir and surrounding liquid. *Microgravity Sci. Technol.* **30**, 353–359. (doi:10.1007/s12217-018-9599-4)
- Tiani R, De Wit A, Rongy L. 2018 Surface tension- and buoyancy-driven flows across horizontally propagating chemical fronts. *Adv. Colloid Interf. Sci.* **255**, 76–83. (doi:10.1016/j.cis.2017.07.020)
- Rongy L, Trevelyan PMJ, De Wit A. 2008 Dynamics of  $A + B \rightarrow C$  reaction fronts in the presence of buoyancy-driven convection. *Phys. Rev. Lett.* **101**, 084503. (doi:10.1103/PhysRevLett.101.084503)

8. Rongy L, Trevelyan PMJ, De Wit A. 2010 Influence of buoyancy-driven convection on the dynamics of  $A + B \rightarrow C$  reaction fronts in horizontal solution layers. *Chem. Eng. Sci.* **65**, 2382–2391. (doi:10.1016/j.ces.2009.09.022)
9. Tiani R, Rongy L. 2016 Influence of Marangoni flows on the dynamics of isothermal  $A + B \rightarrow C$  reaction fronts. *J. Chem. Phys.* **145**, 124701. (doi:10.1063/1.4962580)
10. Budroni MA, Upadhyay V, Rongy L. 2019 Making a simple  $A + B \rightarrow C$  reaction oscillate by coupling to hydrodynamic effect. *Phys. Rev. Lett.* **122**, 244502. (doi:10.1103/PhysRevLett.122.244502)
11. Budroni MA, Polo A, Upadhyay V, Bigaj A, Rongy L. 2021 Chemo-hydrodynamic pulsations in simple batch  $A + B \rightarrow C$  systems. *J. Chem. Phys.* **154**, 114501. (doi:10.1063/5.0042560)
12. Budroni MA, Rossi F, Rongy L. 2021 From transport phenomena to systems chemistry: chemohydrodynamic oscillations in  $A + B \rightarrow C$  systems. *ChemSystemsChem* **3**, e2100023. (doi:10.1002/syst.202100023)
13. Tiani R, Rongy L. 2022 Spatial and temporal oscillations of surface tension induced by an  $A + B \rightarrow C$  traveling front. *Front. Phys.* **10**, 860419. (doi:10.3389/fphy.2022.860419)
14. Guyon E, Hulin JP, Petit L, Mitescu CD. 2001 *Physical hydrodynamics*, 2nd edn. Oxford, UK: Oxford University Press.
15. Nepomnyashchy AA, Velarde MG, Colinet P. 2002 *Interfacial phenomena and convection*, 1st edn. Boca Raton, USA: Chapman and Hall/CRC.
16. Bába P, Rongy L, De Wit A, Hauser MJB. 2018 Interaction of pure Marangoni convection with a propagating reactive interface under microgravity. *Phys. Rev. Lett.* **121**, 024501. (doi:10.1103/PhysRevLett.121.024501)
17. Schwarzenberger K, Eckert K, Odenbach S. 2012 Relaxation oscillations between Marangoni cells and double diffusive fingers in a reactive liquid-liquid system. *Chem. Eng. Sci.* **68**, 530–540. (doi:10.1016/j.ces.2011.10.033)
18. Stergiou Y *et al.* 2022 Effects of gravity modulation on the dynamics of a radial  $A + B \rightarrow C$  reaction front. *Chem. Eng. Sci.* **257**, 117703. (doi:10.1016/j.ces.2022.117703)
19. Rongy L, De Wit A. 2006 Steady Marangoni flow traveling with chemical fronts. *J. Chem. Phys.* **124**, 164705. (doi:10.1063/1.2186313)
20. Trevelyan PMJ, Almarcha C, De Wit A. 2015 Buoyancy-driven instabilities around miscible  $A + B \rightarrow C$  reaction fronts: a general classification. *Phys. Rev. E* **91**, 023001. (doi:10.1103/PhysRevE.91.023001)